Carbonization and Structural Evolution of Bituminous Coal-Derived Carbons Material Toward Supercapacitor Applications

Mohamad Samsul Anrokhi[1], Pipit Fitriani[1], Oktaviardi Bityasmawan Abdillah[2], Fitri Aulia Permatasari[1], Yoshiyuki Yamashita[3,4], Fatimah Arofiati Noor[1], and Ferry Iskandar[1,5*]

[*]ferry@itb.ac.id

[1]*Department of Physics, Faculty of Mathematics and Natural Sciences, Institut Teknologi Bandung, Indonesia 40132*

[2]*Chemical Engineering Program, Department of Advanced Science and Engineering, Graduate School of Advanced Science and Engineering, Hiroshima University*

[3]*Nano Electronics Device Materials Group, Research Center for Electronic and Optical Materials, National Institute for Materials Science, 305-0044 1-1 Namiki Tsukuba Ibaraki, Japan*

[4]*Department of Applied Chemistry, Faculty of Engineering, Kyushu University, Motooka 744, Fukuoka 819-0395, Japan*

[5]*Research Center for Nanoscience and Nanotechnology, Institut Teknologi Bandung, Indonesia 40132*

Abstract

Coal-derived carbon materials have garnered significant interest for energy storage applications due to their abundance, cost-effectiveness, and straightforward processing methods. This study investigates the direct carbonization of bituminous coal at various temperatures (500, 700, and 900 °C) and analysed the evolution of carbon structure, nitrogen functionalities. In addition, the effects on supercapacitor performance were studied. Structural transformations and nitrogen group changes were observed with increasing temperature. At 500°C, pyrrolic-N was the predominant, and it gradually converted to pyridinic-N at 700°C, significantly enhancing charge storage capacity. Further increasing the temperature to 900°C transformed the pyridinic-N into Graphitic-N, improving conductivity. Electrochemical analysis revealed that the sample carbonized at 700°C exhibited the highest specific capacitance of 73.6 F/g, attributed to the high content of pyridinic-N, which contributes to pseudo capacitance via redox reactions. These findings highlight the potential of coal-derived carbon via carbonization as cost-effective and efficient supercapacitor electrode materials. This work demonstrates the importance of optimizing carbonization conditions to balance aromatic carbon structure and nitrogen functionalities for enhanced electrochemical performance.

Keyword: carbonization, coal, functional group, supercapacitor

1. Introduction

Rapid advancement in energy storage technologies has established supercapacitors as crucial components in future energy systems due to their exceptional power density, rapid charge-discharge cycles, and long cycle life [1]. Their capability to bridge the gap between high power output and moderate energy storage makes them essential for applications in electric vehicles, renewable energy systems, and smart power grids [1–3]. However, fully realizing the potential of supercapacitors relies significantly on the development of advanced and cost-effective electrode materials [2]. Various emergent materials such as graphene, MXene, and metal-organic frameworks (MOFs) exhibit remarkable potential, but their high costs and complex synthesis processes limit their widespread applications [4–7].

In response to these challenges, there is increasing interest in more sustainable and cost-effective alternatives, such as coal-derived carbon material. This interest is driven by coal's abundant availability, low cost, and advantageous properties as a precursor for carbon production. Recent progress in coal-derived carbon material toward the supercapacitor application has focused on optimizing various factors such as carbonization temperature, activation methods, and heteroatom doping to enhance electrochemical properties[8–10]. Chemical activation with potassium hydroxide (KOH) or zinc chloride ($ZnCl_2$) and template-assisted approaches have been explored to create porous structures in activated carbon [8, 11, 12]. These methods improve material properties but are often complex and resource-intensive [8, 13]. While activation techniques enhance pseudo-capacitance by introducing acidic surface functionalities, acid activation is suboptimal for carbon-derived materials as it degrades microporosity and diminishes electrochemical performance [14].

Given the limitations of conventional processing techniques, enhancing electrode materials through heteroatom doping has become another popular approach. This technique improves the performance of carbon materials by incorporating elements such as Nitrogen, Sulphur, or Boron into the carbon lattice, leading to significant enhancements in physicochemical properties [15–18]. Nitrogen doping effectively enhances the electronic conductivity, charge storage capacity, and surface wettability of coal-derived carbon materials. This is achieved through the formation of π-conjugated systems with carbon atoms, which modify local charge density, improve electron transport, and increase hydrophilicity, thereby boosting overall electrochemical performance [19–22]. The type and concentration of nitrogen dopants (e.g., pyridinic-N, pyrrolic-N, or graphitic-N) are crucial for optimizing electronic performance. Previous studies reported that the introduction of small amount of nitrogen atoms (< 2 wt.%) into coal-derived carbon material can significantly enhance performance of supercapacitor electrodes [23, 24]. However, in these reports, the nitrogen-containing precursors were intentionally added into carbon materials for introducing nitrogen doping, which complicates the experimental procedure. Meanwhile, coal in its bare form also offers a distinct advantage by inherently possessing approximately 1-2 wt.% nitrogen within their structure, primarily in the form of heterocyclic rings [22]. This inherent nitrogen content offers a distinct advantage by enabling the enhancement of material properties for supercapacitor electrode applications without requiring additional doping steps.

Moreover, it simplifies the preparation process while complementing the carbon structure, which consists of aromatic and aliphatic components, each playing a distinct role in defining the physicochemical properties of coal-derived carbon materials. Aromatic carbons, with their planar ring structures and delocalized π-electrons, contribute significantly to stability and conductivity. Conversely, aliphatic carbons, characterized by their chain-like structures, enhance flexibility and surface area [25]. To effectively enhance the performance of supercapacitor electrode, controlling the aromaticity and nitrogen configuration in coal is essential to achieve a balance between excellent electron transport, increased wettability, and additional charge storage capability [1][3]. Therefore, understanding the chemistry of this relationship could be crucial for achieving effective outcomes.

The pyrolysis of coal, commonly referred to as carbonization, serves as a fundamental process for this purpose. Conducted under oxygen-free conditions and without the need for chemical additives, it enables the detailed study of the evolution of carbon bonding, the behaviour of organic atoms such as nitrogen and oxygen, and the transformation of mineral phases. These insights are crucial for elucidating the relationship between nitrogen configurations, carbon structures, and their impact on the electrochemical performance of supercapacitor materials [26–28]. Previous studies have been conducted to investigate structural changes of coal under various carbonization temperatures. Li et al. [29] observe the alterations to the stacking structure that happened when low-rank coals were heated to 900°C. The observation showed that the increase in temperature affects the change in crystal parameters of aggregate structure of low-rank coal. Meanwhile, Xu et al. [30] develop and use micro-Raman spectroscopy to examine alterations in the char structure produced during the pyrolysis of Zhundong coal. According to the results, the char becomes more crystalline and thermally stable at high temperatures because they improve the order of carbon structures. On the other hand, study by Meng et al. [31] about pyrolysis-induced modifications to coal's carbon structure and functional groups shows that at temperatures below 1000°C, the coal particles' surface and core experiences distinct changes in the aromatic rings' structure. In the meanwhile, comparable changes often occur in the functional groups. At 1000°C, the functional groups especially the aliphatic C-H in the centre are slightly altered and nearly all of them break down on the surface, while the big and tiny aromatic ring structures significantly increase. Alongside examining the development of carbon structure and its functional groups, carbonized coal has been utilized for application as an anode in lithium and sodium ion batteries

which can provide the specific capacity of 384 $mAhg^{-1}$ at 0.1C and 270.1 $mAhg^{-1}$ at 0.1C, respectively [32]. In addition, the research conducted by Yang et al. focused on the transformation of nitrogen functional groups in *Chlorella vulgaris*-derived biochar under different pyrolysis temperatures, demonstrating that specific nitrogen functionalities can serve as active sites for the oxygen reduction reaction (ORR) application [33]. While their work contributed valuable insights into nitrogen chemistry in biochar, our study extends this scope by exploring the concurrent evolution of both inherent nitrogen functionalities and carbon structure and understanding how these structural changes influence the electrochemical performance of the resulting carbon material when applied as a supercapacitor electrode.

In this study, direct carbonization of bituminous coal was performed at 500, 700, and 900°C to investigate structural changes in carbonized coal. The alterations in carbon structure are anticipated to improve the electrochemical characteristics as a supercapacitor electrode. By fine-tuning carbonization conditions, we aim to achieve a favorable balance of high aromatic carbon content, suitable aliphatic carbon levels, and enhanced nitrogen functionalities, without additional doping and activation steps. Unlike previous studies by Cheng et al. [34], which focused solely on carbon structure, and Niu et al. [35], which examined only the thermal behaviour of functional groups, our work explores the interplay between these factors. This study demonstrates how these elements can improve supercapacitor performance and offer a cost-effective solution for advanced energy storage applications.

2. Experimental section

2.1 Preparation and Carbonization of Bituminous Coal

The bituminous raw coal used in this study was sourced from PT. Bukit Asam, Indonesia and classified as high-volatile bituminous-B based on proximate and ultimate analyses. It exhibited 39.57 wt.% volatile matter and 1.35 wt.% nitrogen, as detailed in a previous study [33]. These properties are important since the high volatile matter enhances the yield and porosity of the carbonized material while the inherent nitrogen facilitates nitrogen doping without additional processing. Prior to the carbonization process, the raw coal was ground and sieved to achieve a particle size of approximately 200 μm. The raw coal powder was then dried in an oven at 110°C for 2 hours to remove moisture content. Following drying, the coal powder was subjected to carbonization in a tubular furnace at temperatures ranging from 500 to 900°C for 2 hours in a 0.4

l/m flow rate of Ar atmosphere. The carbonized coal produced at varying temperatures (500, 700 and 900°C) were labeled as C-500, C-700, and C-900, respectively, while the uncarbonized raw coal was labeled as RC.

2.2 Characterization

The infrared spectroscopy analysis was conducted to identify functional groups using IR Prestige-21 Shimadzu covering the wavenumber range from 400-4500 cm^{-1} using the KBr pellet technique. Raman spectroscopy was employed through a MacroRam benchtop using a 532 nm laser to identify and quantify defects within the structure. X-ray Diffraction (XRD) used to identify the crystalline phase was performed using a Bruker D8 Advance diffractometer, utilizing a Cu K-α radiation source (λ=0.15418 nm). In addition, carbon surface chemistry measurements were performed using a X-ray photoelectron spectroscopy (XPS) HI Quantes (ULVAC-PHI) instrument using a photon energy of 1486.6 eV Al Kα to determine the surface chemistry of samples with the energy resolution of 0.51 eV.

2.3 Electrochemical measurement

The working electrodes were prepared by mixing 80 wt.% carbonized coal, 10 wt.% carbon black, and 10 wt.% polyvinylidene fluoride (PVDF) in 1-methyl-2-pyrrolidinone (NMP) to form a slurry. This slurry was then coated onto a nickel foam current collector (1 cm × 1 cm). The coated electrodes were dried at 100°C for 12 hours in a vacuum oven. Electrochemical properties were assessed using a three-electrode setup under ambient conditions, with a platinum mesh and an Ag/AgCl electrode serving as the counter and reference electrodes, respectively. Cyclic voltammetry (CV), and galvanostatic charge-discharge (GCD) were performed using a Parstat 3000A electrochemical workstation in a 3 M KOH electrolyte at room temperature. The specific capacitance (S_C) value obtained from galvanostatic charge-discharge (GCD) was determined using the equation below [34]:

$$S_C = \frac{I\Delta t}{m\Delta V} \quad (1)$$

3. **Results and Discussions**

Materials Characterization

Fig. 1 shows the X-ray diffraction (XRD) patterns of carbonized coal samples subjected to various carbonization temperatures. The patterns reveal a pronounced background intensity, indicating a significant amount of amorphous carbon and considerable structural disorder within the carbonized coal [35]. Diffraction peaks identified at 2θ value of 20.9°, 26.7°and 50.1° are assigned to the crystal structure of SiO_2 (quartz) based on JCPDS no 46-1045 [36] These diffraction peaks correspond to the inorganic crystalline mineral phases inherently present in the raw coal. Additionally, two main broad diffractions are observed around the 2θ = ~23°and 43°, which corresponds to the (002) and (100) plane of carbon. The first peak centered in the 23°, corresponds to the reflection of the microcrystalline (002) plane and arises from the stacking of aromatic layers. The second broad peak, located at approximately 43°, is attributed to the (100) plane and denotes the presence of graphite-like atomic arrangements within the individual layers [35, 37]. Furthermore, the Gaussian fitting method was employed to assess the asymmetry of the (002) peak, enabling precise deconvolution of overlapping signals to reveal the coexistence of ordered and disordered carbon structures, as well as provide quantitative insights into stacking, crystallite size, and phase distribution [38]. The representative Gaussian fits for the bands in the coal samples are illustrated in **Fig. 1(b-d)**. This analysis revealed that the presence of an additional band around 15°, attributed to the γ band, which arises from saturated aliphatic sidechains attached to the edges of coal crystallites [38, 39]. The interlayer spacing (d002) calculated using Bragg's equation (Eq. 2) reveals the degree of graphitization. Meanwhile, the peak positions and the full width at half maximum (FWHM) values obtained from Gaussian fitting of the 100 and 002 peaks from the XRD patterns were used to calculate the lateral size (La) and stacking height (Lc) based on Scherrer equation (Eq.3) and (Eq.4), respectively [29]. Additionally, aromaticity is determined from the area under the (002) and γ bands as calculated using Eq. 5, representing the ratio of carbon atoms in aromatic rings to those in aliphatic chains [27].

$$d_{002} = \frac{\lambda}{2sin\,\theta_{002}} \tag{2}$$

$$L_a = \frac{1.84\lambda}{\beta_{100}\cos\theta_{100}} \tag{3}$$

$$L_C = \frac{0.9\lambda}{\beta_{002}\cos\theta_{002}} \tag{4}$$

$$f_a = \frac{C_{ar}}{C_{al}} = \frac{A_{002}}{A_{002}+A_\gamma} \quad (5)$$

where λ is the wavelength of the X-ray (1.5406 Å), and θ_{002} and θ_{100} are the peak positions of 002 and 100 bands, respectively. A_{002} and A_γ are the integrated areas of 002 and γ bands, respectively. The peak positions and the calculated results of Eqs. (2), (3), (4), and (5) are summarized in Table 1.

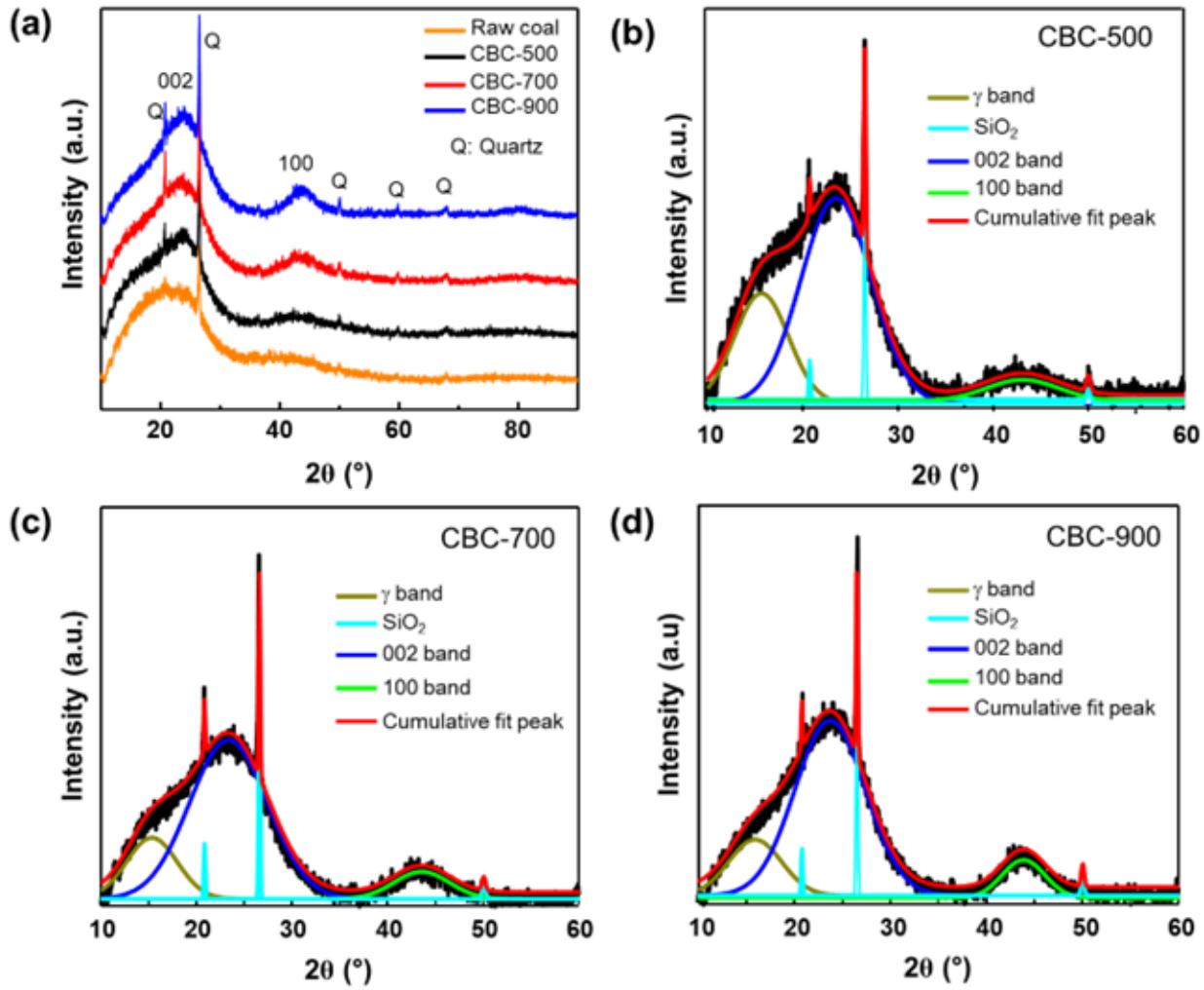


Fig. 1 (a) XRD patterns of coal subjected at different carbonization temperatures; the curve fitting of the XRD spectra of (b) CBC-500, (c) CBC-700, and (c) CBC-900

As the carbonization temperature increases, the (002) and (100) peaks in the XRD patterns exhibit a slight shift to higher angles, indicating changes in the interlayer spacing. While these shifts suggest some degree of structural reorganization towards a more ordered graphite-like structure, the broad nature of the (002) and (100) peaks across all samples highlights the significant

presence of turbostratic carbon. Additionally, mineral peaks are observed in Figure 1, with quartz (SiO_2) being the most prominent mineral detected in all samples. The observed increase in L_a with higher temperatures reflects the expansion of aromatic domains, as the thermal energy facilitates the growth of aromatic rings, contributing to improved electron transport and structural stability. However, a decrease in L_c at 700°C compared to 500 and 900°C suggests a transitional phase in the carbonization process, where the decomposition of aliphatic groups and volatile components temporarily disrupts vertical stacking, but lateral ordering progresses undisturbed resulting imbalance at temperature 700°C represents an intermediate stage in the carbonization process. Furthermore, the increase in aromaticity (f_a) with temperature highlights the progressive conversion of aliphatic carbon to aromatic structures, enhancing conductivity and stability [32].

Table 1. The peak positions, d_{002}, L_c, L_a, f_a and Unit cell of CBC-500, CBC-700 and CBC-900

Sample	$2\theta_{002}(°)$	$2\theta_{100}(°)$	d_{002} (Å)	L_a (Å)	L_c (Å)	$f_a(\%)$	Unit Cell (Å^3)
CBC-500	23.50	43.07	3.78	19.49	9.32	70.68	38.52
CBC-700	23.31	43.52	3.81	25.75	8.47	79.90	38.00
CBC-900	23.74	43.84	3.74	33.41	9.38	80.67	36.83

To elucidate the molecular structure and functional groups of coal before and after the carbonization process, the FTIR spectra of the coal samples were analyzed and categorized into four functional group regions: hydroxyl groups (3600 - 3000 cm^{-1}), aliphatic groups (3000 - 2700 cm^{-1}), oxygen-containing functional groups (1800 - 1000 cm^{-1}), and aromatic groups (900 - 700 cm^{-1}) [40]. As shown in **Fig. 2**, the carbonization process leads to a decrease in the intensity of the peaks corresponding to all four functional group regions, while the peak positions remain largely unchanged. In the hydroxyl region (3600 - 3000 cm^{-1}), all samples exhibit a broad, intense band, which diminishes in intensity with increasing carbonization temperature. This reduction is attributed to the loss of hydroxyl (-OH) and amino (-NH) groups [41]. The aliphatic region (3000 - 2700 cm^{-1}), which primarily consists of methyl (-CH_3), methylene (-CH_2), and methine (-CH-) groups, also shows a marked decrease in peak intensity. These aliphatic groups are less thermostable due to their lower binding energies, making them more prone to degradation at higher temperatures [42]. Finally, the peaks in the 956 - 1050 cm^{-1} range correspond to C-O-C functional groups [43]. The CBC-700 sample exhibits a notably sharper peak in this region compared to the

CBC-500 and CBC-900 samples, indicating structural reorganization of oxygen-containing functional groups. The overall trends in the FTIR spectra demonstrate that increasing the carbonization temperature significantly transforms the molecular structure of coal, primarily through the removal of aliphatic and hydroxyl functional groups and the rearrangement of aromatic structures. These transformations yield a more thermally stable and structurally ordered carbon material, which is essential for enhancing the performance of carbonized coal in various applications.

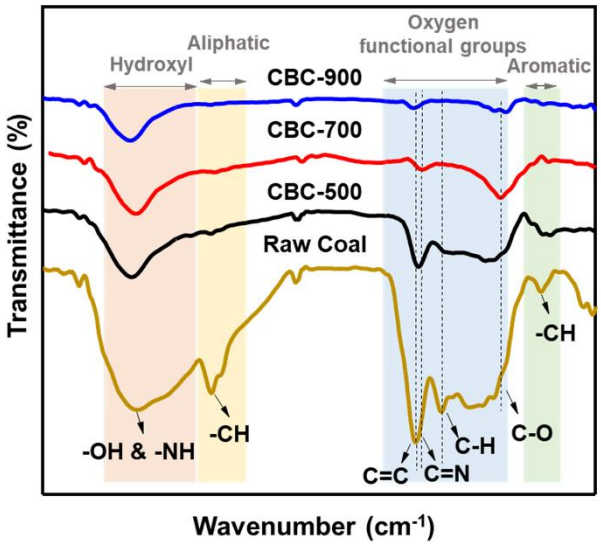


Fig. 2 FTIR spectrum of carbonized-coal samples at different temperatures

Furthermore, Raman spectroscopy was used to assess the degree of structural disorder and graphitization in the carbonized coal samples. **Fig. 3(a)** presents the Raman spectra of coal samples subjected to carbonization at various temperatures. The spectra exhibit two prominent broad and overlapping peaks centered at 1358 and 1585 cm^{-1}, corresponding to the D and G bands of disordered graphite, respectively. The D band at 1358 cm^{-1} is indicative of defects and disorder within the graphite structure, primarily arising from the breathing modes of sp^2 atoms in aromatic rings. In contrast, the G band at 1585 cm^{-1} is associated with the in-plane vibrations of sp^2-bonded carbon atoms in graphite-like materials [44]. These observations confirm the presence of significant structural disorder in the carbonized coal samples, consistent with the typical Raman spectral characteristics of disordered and amorphous carbon materials [44]. The Raman results complement the FTIR findings, highlighting the structural transformations observed in both analyses. The reduction in aliphatic and oxygen-containing functional groups in the FTIR spectra

corresponds to a decrease in the Raman spectral intensity with increasing temperature. Together, these results indicate the removal of structural defects and oxygenated components, along with the progressive formation of more ordered aromatic carbon structures during carbonization. In addition, the relatively broad D and G bands across all carbonized coal samples suggest a small carbon crystallite size [39]. To gain deeper insights into the structure of carbonized coal, Raman spectrum deconvolution was employed. The overlap of the D and G bands tends to obscure critical structural details [45]. Among the available deconvolution techniques, the method combining Lorentzian and Gaussian functions, as proposed by Sadezky et al. [46] has been identified as the most suitable for these samples. The results of this deconvolution are presented in **Fig. 3(b-d)**, with the five deconvoluted bands and their assignments succinctly summarized in Table 2.

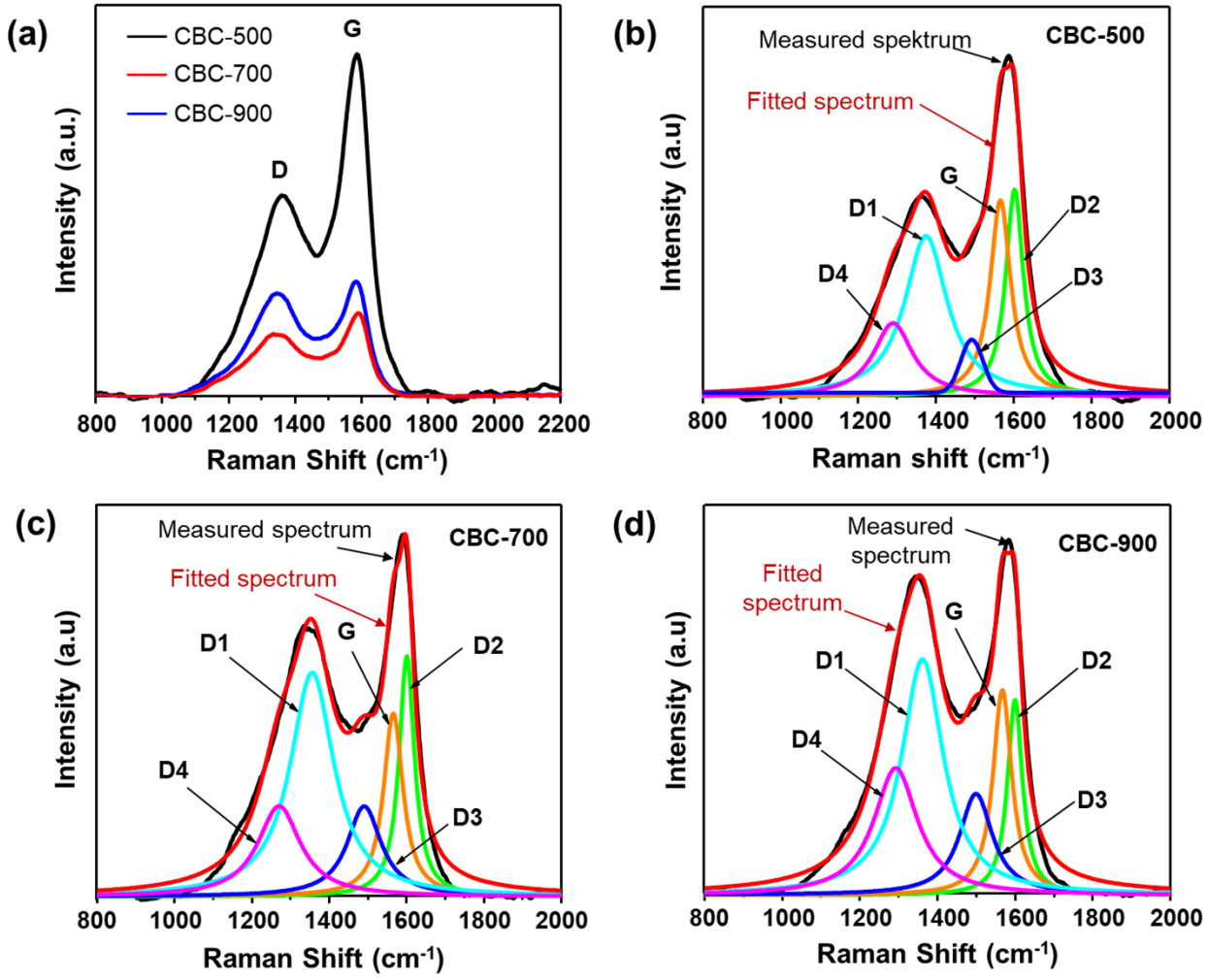


Fig. 3 (a) Raman spectrum of carbonized coal; deconvolution of (b) CBC-500, (c) CBC-700, and (d) CBC-900

Table 2. The five bands resulting from the fitting deconvolution in the Raman spectra [44, 46–49]

Band name	Band position (cm^{-1})	Description
G	1565 (CBC-500) 1565 (CBC-700) 1567 (CBC-900)	Ideal graphitic lattice (E_{2g} symmetry)
D1	1374 (CBC-500) 1355 (CBC-700) 1361 (CBC-900)	Disordered graphitic lattice, (graphene layer edges, A_{1g} symmetry)
D2	1601 (CBC-500) 1600 (CBC-700) 1599 (CBC-900)	Disordered graphitic lattice, (surface graphene layer edges, E_{2g} symmetry)
D3	1492 (CBC-500) 1500 (CBC-700) 1491 (CBC-900)	Amorphous carbon
D4	1289 (CBC-500) 1269 (CBC-700) 1292 (CBC-900)	Disordered graphitic lattice, (A_{1g} symmetry)

Based on the data presented in Table 2 and the amorphization trajectory discussed in the previous study [44], the position of the G peak (1600-1510 cm^{-1}) suggests that the CBC samples exhibit structural characteristics intermediate between nanocrystalline graphite and amorphous carbon. This observation indicates that the samples comprise a combination of highly disordered carbon and partially ordered graphitic domains. As the carbonization temperature increases, the G band wavenumber is relatively stable, with only minimal shift observed at 900°C while the D1 band tends to shift toward lower wavenumbers. This shift indicates a gradual transition from amorphous to more ordered graphitic structures. If the carbonization temperature continues to increase towards the graphitization temperature (1700-2900°C), it is expected that the G band will approach a band position of 1580 cm^{-1} and the D1 band will reach approximately 1300 cm^{-1}, which are characteristic of disordered graphitized carbon [50]. These trends underscore the influence of temperature on the structural evolution of carbonized coal, highlighting the potential to tailor material properties by controlling the carbonization process.

The area ratios of the D_1 band to the G band (I_{D1}/I_G) and the G band to the total area (I_G/I_{All}) are critical metrics for assessing the degree of order within the carbon structure. Specifically, the I_{D1}/I_G ratio is inversely related to the plane size of the carbon crystals, where a decrease in I_{D1}/I_G

signifies an increase in structural order[51, 52]. Conversely, the G peak representing the vibrational mode of aromatic compounds, becomes more pronounced with a higher I_G/I_{All} ratio, indicating a more ordered carbon structure [51, 52]. As illustrated in **Fig. 4**, an increase in the carbonization temperature from 500 to 700°C results in the I_{D1}/I_G value rising from 1.69 to 2.76. However, when the temperature is further elevated to 900°C, the I_{D1}/I_G value decreases slightly to 2.55. Simultaneously, the I_G/I_{All} value decreases from 0.221 to 0.150 as the temperature rises from 500°C to 700°C, but this trend reverses slightly with an increase to 0.155 at 900°C. In the range temperature of 500 and 700°C, dehydrogenation of hydroaromatic compounds and the formation of aromatic rings increase the aromatic content. Despite this, the structure remains highly disordered and differs significantly from graphite crystals. The polycondensation process breaks downside chains and produces small molecules that deposit on the coal surface. This deposition introduces defects and amorphous structures, disrupting carbon regularity. As the temperature rises, these defects and amorphous regions gradually transform into more ordered structures. It reflects a balance between disorder and the development of graphite-like domains at higher temperatures. The change of $(I_{D3}+I_{D4})/I_G$ is regarded as crosslinking density related to the formation of alkyl-aryl C-C. There is a fast increase in $(I_{D3}+I_{D4})/I_G$ in the 500 - 700°C temperature range due to the release of functional groups as small molecular entities, which promotes the formation of alkyl-aryl C-C bonds. Meanwhile, the rise slows between 700 and 900°C because the release of functional groups as tiny molecular substances reduces, impacting the creation of $(I_{D3}+I_{D4})/I_G$.

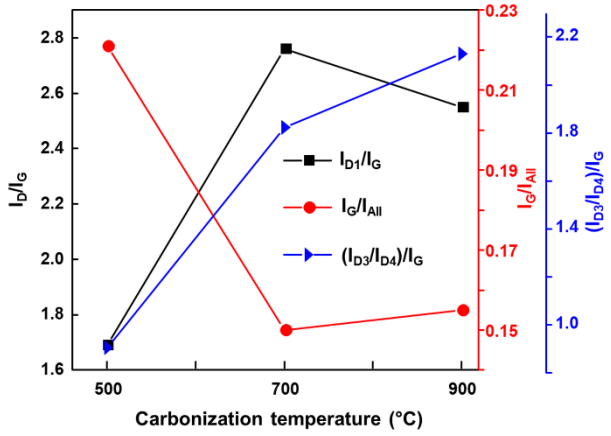
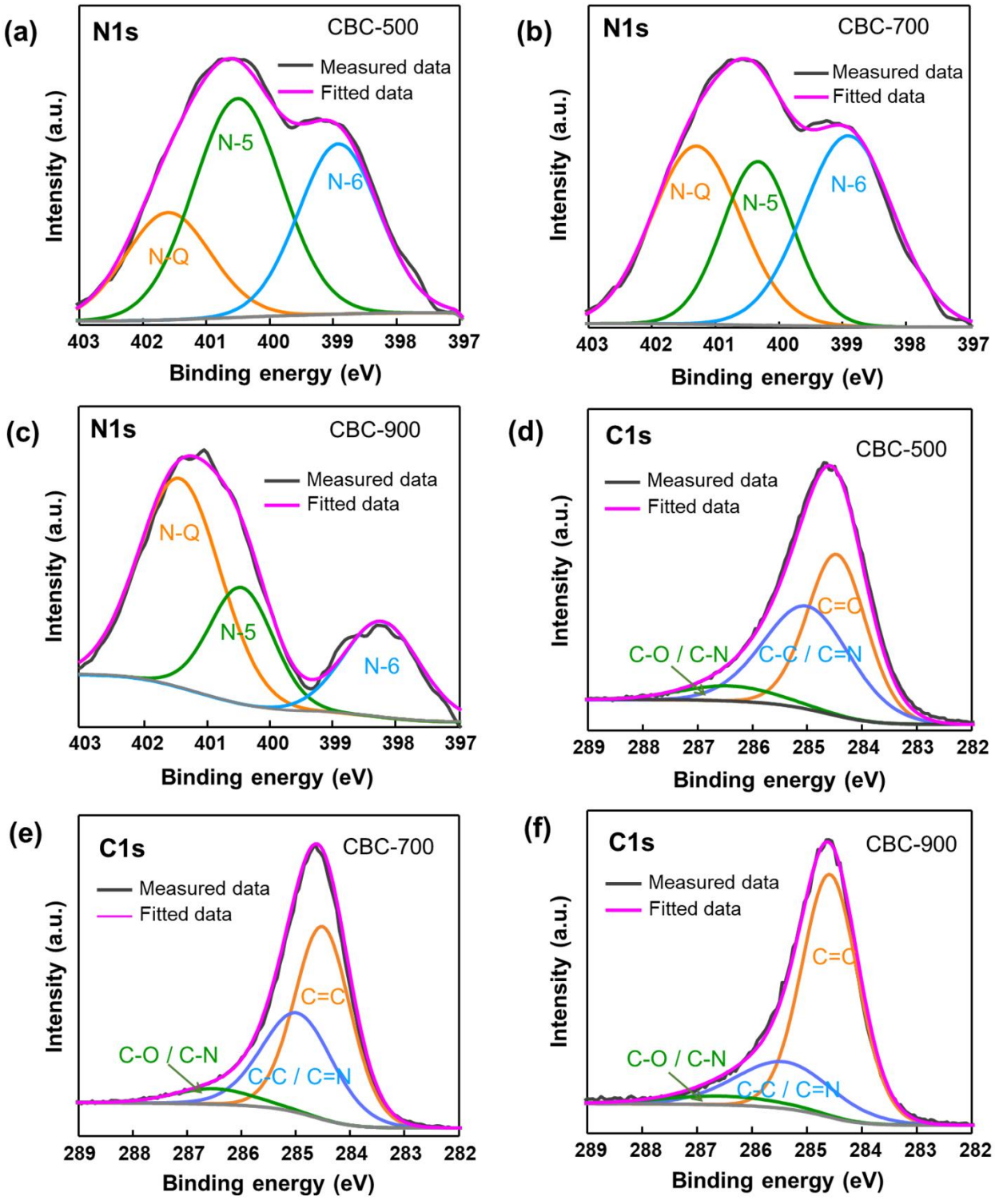


Fig. 4 Evolution of structural parameters obtained from Raman spectroscopy characterization in carbonized coal

1


(a)
N1s
CBC-500
Measured data
Fitted data
N-5
N-6
N-Q
Intensity (a.u.)
403 402 401 400 399 398 397
Binding energy (eV)
(b)
N1s
CBC-700
Measured data
Fitted data
N-Q
N-5
N-6
Intensity (a.u.)
403 402 401 400 399 398 397
Binding energy (eV)
(c)
N1s
CBC-900
Measured data
Fitted data
N-Q
N-5
N-6
Intensity (a.u.)
403 402 401 400 399 398 397
Binding energy (eV)
(d)
C1s
CBC-500
Measured data
Fitted data
C=C
C-O / C-N
C-C / C=N
Intensity (a.u.)
289 288 287 286 285 284 283 282
Binding energy (eV)
(e)
C1s
CBC-700
Measured data
Fitted data
C=C
C-O / C-N
C-C / C=N
Intensity (a.u.)
289 288 287 286 285 284 283 282
Binding energy (eV)
(f)
C1s
CBC-900
Measured data
Fitted data
C=C
C-O / C-N
C-C / C=N
Intensity (a.u.)
289 288 287 286 285 284 283 282
Binding energy (eV)

2

Fig. 5 High resolution XPS spectra of C1s and N1s peaks obtained from (a,d) CBC-500, (b,d) CBC-700, and (c,f) CBC-900, respectively. N-Q, N-5, and N-6 correspond to quaternary, pyrrolic, and pyridinic configuration of nitrogen atoms bonded with carbon atoms

Table 3. Quantitative analysis of chemical bonds obtained by deconvolution of C1s XPS spectra

Sample	C=C/C-C (at. %)	C-OH/C=N (at. %)	C-O / C-N (at. %)
CBC-500	47.75	44.97	7.28
CBC-700	56.50	37.21	6.28
CBC-900	70.94	23.77	5.29

Table 4. Quantitative analysis of chemical bonds obtained by deconvolution of N1s XPS spectra

Sample	Pyridinic / N-6 (at. %)	Pyrrolic / N-5 (at. %)	Quaternary / N-Q (at. %)
CBC-500	32.54	45.76	21.69
CBC-700	38.63	25.95	35.42
CBC-900	22.68	23.36	53.96

XPS analysis was utilized to further study the surface chemical bonds of the as-synthesized CBC samples. Full scan XPS of all samples shown in **Fig. S1** exhibit 7 peaks, attributed to the C 1s, C KLL, O1s, O KLL, N 1s, Si 2s, and Si 2p peaks. It is evident that in addition to the carbon and oxygen constituents commonly found in coal-derived samples, trace quantities of nitrogen and silicon elements are also present across all samples. The detection of silicon is consistent with the X-ray diffraction data, which reveals the presence of SiO_2 in every sample analyzed. Then, the quantification of each element is depicted in Table S1. It reveals that increasing carbonization temperature from 500 to 700°C escalates the carbon content in the CBC sample while the O element decreases, and N element remain stable. The decrease in O element is caused by decomposition of oxygen-containing functional groups in coal sample owing to elevated temperature [53]. However, further increasing of temperature to 900 °C induces decomposition of carbon species to CO_x gas ultimately decreasing of carbon composition in CBC-900 [54]. The SiO_2 remains stable at 900°C [55,56], however as N and C decompose, the relative concentrations of Si and O increase. Similar concepts of interaction-guided performance tuning have also been explored in ionic hydrogel systems [55].

The high resolution of C 1s and N 1s peaks from XPS spectra were demonstrated in **Fig. 5** (a) and (b). In C 1s spectrum, the C=C peak (~ 284 eV) increases gradually as temperature and is followed by decreasing amount of nitrogen and oxygen-containing functional groups (C-OH, C-

O, C-N, and C=N) (Table 3). It suggests the reduction of functional groups during carbonization process leading to an increasing amount of aromatic carbon. This phenomenon is in accordance with XRD result that higher carbonization temperature causes high aromaticity of CBC sample. Besides, the deconvolution of N 1s peaks also reveals that the evolution of nitrogen species contained in carbonized coal has also occurred as increasing carbonization temperature.

The CBC-500 is dominated by N-5 (pyrrolic) followed by N-6 (pyridinic) and N-Q (quaternary) configuration. When the carbonization temperature increased to 700 °C, pyrrolic content is decreased, while the pyridinic and graphitic content increased. This evolution involves dehydrogenation, aromatization and carbon restructuration as an increase of heating temperature [56]. Further escalation of temperature to 900 °C caused pyridinic nitrogen to be reduced as does the pyrrolic which continuously decreased. Meanwhile, the quaternary continues to increase due to transformation of pyridinic to graphitic in high temperature[56, 57]. The XPS results reveal that heating temperature can easily tune the amount and configuration of oxygen and nitrogen species in the carbonized coal.

Surface area and pore distribution analysis.

The porosity characteristic of carbonized coal were measured via N_2 adsorption-desorption isotherm. The detailed parameter information is presented in Table 5.

Table 5. the pore structure parameters of obtained by N_2 (77.3 K)

Sample	S_{Bet} (m^2g^{-1})	V_{tot} (cm^3g^{-1})	D_{avr} (nm)
CBC-500	**0.087**	**0.001**	**30.4**
CBC-700	**4.277**	**0.008**	**7.14**
CBC-900	**2.541**	**0.006**	**4.55**

As shown in table 5, S_{BET} increases rapidly from 0.087 to 4.277 m3g-1. This indicates that the release of small molecules at around 700°C provides an advantage for pore structure formation. Subsequently, S_{BET} decreases at 900°C due to the collapse of pores[58]. The pore size distribution of all samples by using BJH method are shown in Fig.6. the CBC-500 shows pore size distribution dominate around 30.4 nm.

Although 500°C is a low temperature, the pore size and analysis of pore size distribution shows the largest pore size, which is around 30.4 nm, with the pore size distribution only around that pore size. At 500°C, it is the initial decomposition process that releases volatile gases and creates a large pore structure. However, because the temperature is not sufficient for significant aromatization and graphitization, the pores remain open and do not experience narrowing. Conversely, at higher temperatures (700 and 900), there is an increase in the degree of aromatization, which causes the pores to narrow.

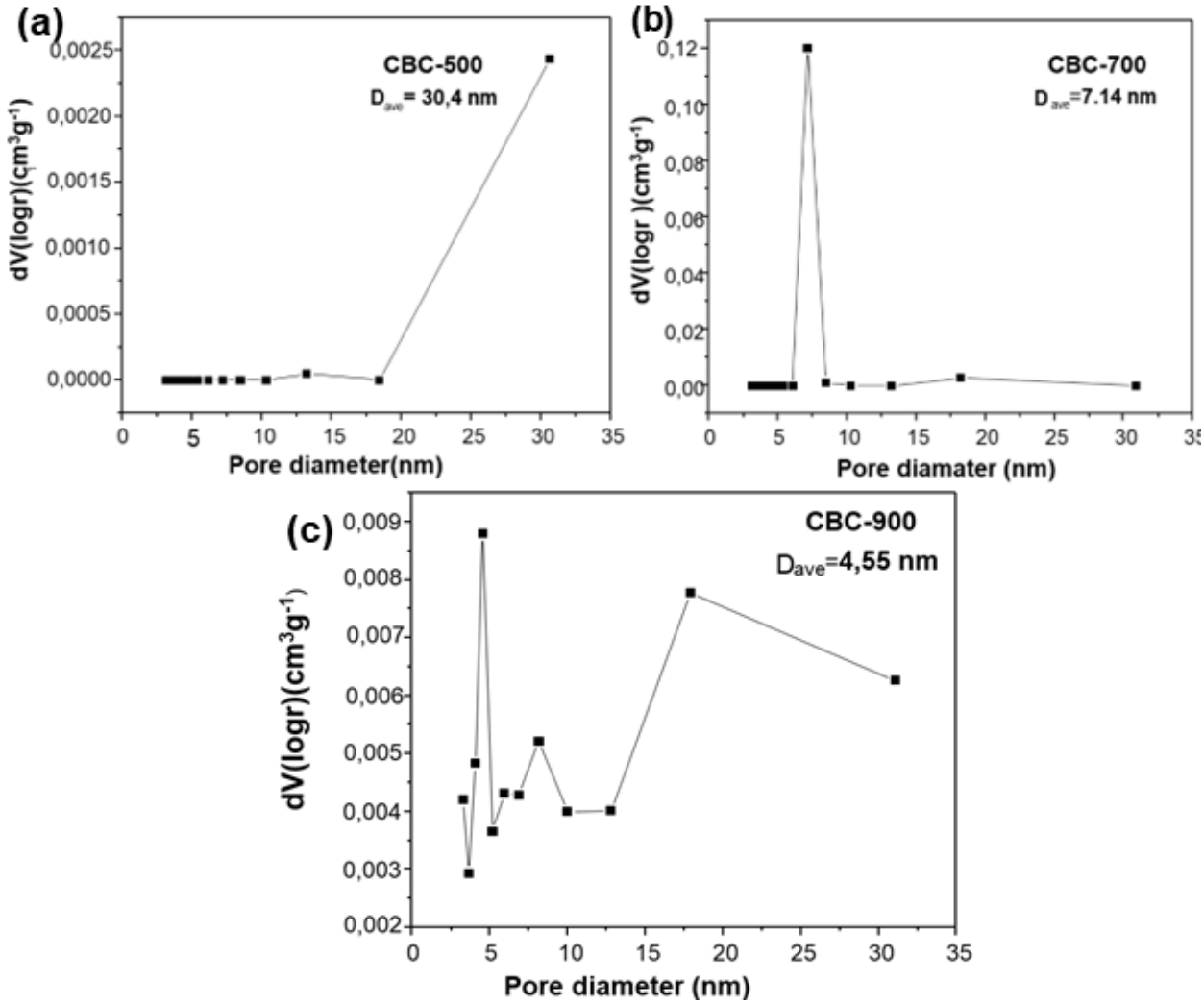


Fig. 6 Pore size distribution (a) CBC-500, (b) CBC-700 (c) CBC-900

Electrochemical Characteristics

The electrochemical characteristics of CBC samples were evaluated in a 3M KOH aqueous electrolyte at ambient temperature using a three-electrode supercapacitor cell. **Fig. 6(a)** shows the

cyclic voltammetry (CV) results of CBC samples within the voltage range -0.2 to -1.0 V at a scan rate of 10 mV/s. The CV curves exhibit capacitive behavior typical of electrical double-layer capacitors. The area inside CV curve of CBC-700 is notably more rectangular and wider compared to those of CBC-500 and CBC-900. This suggests that CBC-700 exhibits superior capacitive behavior and charge propagation at the electrode surface, indicative of enhanced electric double-layer capacitance.

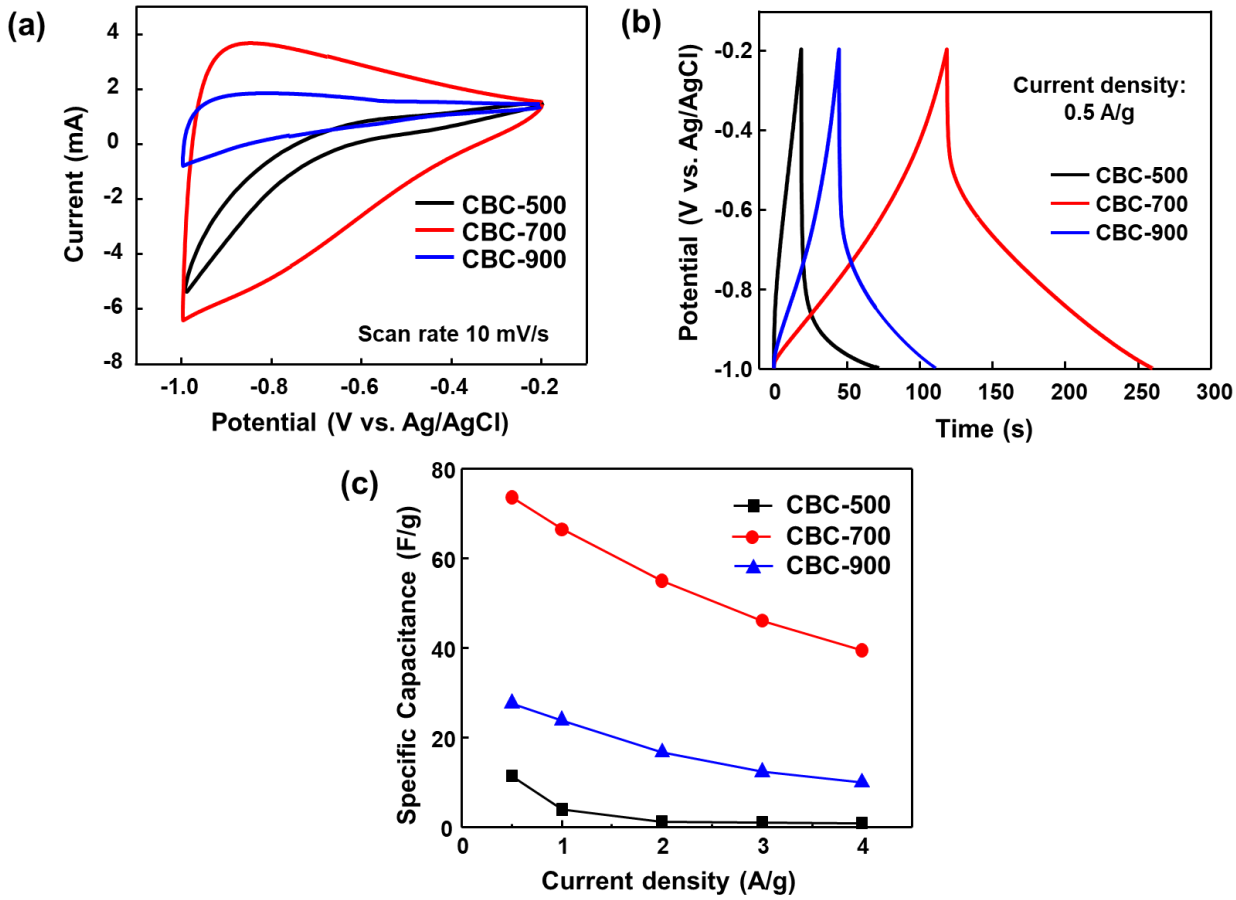


Fig. 7 Electrochemical performance of CBC prepared under various carbonization temperatures including (a) CV data from -1.0 to -0.2 V vs. Ag/AgCl at scan rate of 10 mV/s, (b) GCD data from -1.0 to -0.2 V vs. Ag/AgCl at 0.5 A/g, and (c) rate capability obtained from GCD at various current densities

Galvanostatic charge-discharge tests were carried out on each sample to further assess their electrochemical capabilities within the voltage range -0.2 V to -1.0 V, employing a current density of 0.5 A/g. GCD curves as shown in **Fig. 7 (b)** showed non-ideal triangular shape profiles. The specific capacitance (S_C) of all samples was calculated from GCD curves by using the equation 2.

The corresponding capacitance from discharge is 1.98, 11.4, 73.6, and 27.7 F/g of Raw coal, CBC-500, CBC-700, and CBC-900, respectively. The CBC-700 possesses the highest specific capacitance value, attributed to the contribution of the nitrogen moieties as shown in XPS results. The presence of the nitrogen moieties improves the wettability of the electrode due to an elevated hydrophilic polar site [59]. It allows electrochemical reactions to occur more efficiently due to enhance electrode-electrolyte contact. In addition, among the different types of N, the pyridinic-N plays a role in the contribution of additional pseudo capacitance from redox reactions, especially in basic media [60]. Meanwhile, graphitic-N enhances capacitive performance by altering the electronic structure of carbon to be more conductive [61]. On the other hand, pyrrolic-N reduces the normalized capacitance while pyridinic-N increases the normalized capacitance [62]. Under negative voltage, pyridinic-N and graphitic-N can store charge better than pyrrolic-N. On the contrary, pyrrolic-N does so at positive potential [63]. Given that aqueous-based electrolytes are used in this study, the electrode's water absorption capacity becomes critical, as it influences wettability, ion transport, and electrochemical properties.

The specific capacitance values of CBC-500, CBC-700, and CBC-900 measured under various current densities are displayed in **Fig. 7 (c)**. The specific capacitance of CBC samples is reduced as the current density increased from 0.5 A g^{-1} to 4 A g^{-1} as shown in **Fig. 6 (c)**, which was connected to the limited movement of electrolyte ions on the electrode material surface during fast charging [64]. After the charge-discharge measurement at 4 A g^{-1}, the specific capacitance of these electrodes remains 11.58, 53.65, and 36.11 F/g compared to the specific capacitance at 0.5 A g^{-1}. The carbonization process at 500°C still obtains a low aromaticity of coal and low interlayer spacing which is not favorable for electron transfer which causes a low-rate capability of electrode. When the temperature of carbonization increases to 700°C, the better capability of electrode can be obtained as the higher remaining specific capacitance is still observed. It is attributed to combination of several effects, such as high aromaticity, large interlayer distance, and good wettability of carbonized coal owing to dominant N-pyridinic content as resulted from XRD and XPS measurement [65]. These effects facilitate faster electrolyte ions and electrons during the charge-discharge process, thus when high current densities are applied, they can induce higher specific capacitance. Meanwhile, although further increasing carbonization temperature to 900°C can improve the aromaticity degree of coal, structural changes in carbon at that temperature affect surface area, pore size, and functional groups, all of which affect capacitance values. As

demonstrated in Table 5, and Figure 6 depicts the pore size distribution. The specific surface area and pore size of CBC-900 are smaller than those of CBC-700, as is the number of pyridinic-N functional groups decreases which is less favorable for ionic penetration into active sites for charge storage. It induces the imbalance electron and ionic transport which results in lower capability of CBC-900 than CBC-700 [65]. These results reveal that different heating temperatures of coal can affect the electrochemical properties of supercapacitor electrodes that are related to the changing of structural and chemical bonds during carbonization process.

Conclusion

This study investigated the effects of carbonization temperature on nitrogen transformation, structural properties, and the specific capacitance performance of coal-derived carbon materials. The results demonstrated that carbonization temperature significantly influences coal's molecular structure, with higher temperatures increasing aromaticity and altering nitrogen configurations. At 500°C, pyrrolic nitrogen was the dominant functional group and it transformed into pyridinic nitrogen at 700°C, which contributed to the highest specific capacitance of 73.6 F/g. At 900°C, graphitic nitrogen became more prevalent, enhancing conductivity but reducing charge storage performance. The findings highlight CBC-700 as the optimal material for supercapacitor electrodes, emphasizing the role of pyridinic nitrogen in achieving superior capacitance.

Acknowledgment

This work was fully supported by the Ministry of Finance, Republic of Indonesia, through the Endowment Fund for Education (LPDP) for doctoral scholarship program.

CRediT Authorship contribution statement

Mohamad Samsul Anrokhi: Conceptualized the study, conducted the experiments, performed data collection and analysis, and drafted the initial manuscript.
Pipit Fitriani: Contributed data analysis and interpretation and assisted in manuscript preparation.
Oktaviardi Bityasmawan Abdillah: Supported data analysis and participated in manuscript drafting.
Fitri Aulia Permatasari: Reviewed the manuscript and provided revisions.
Yoshiyuki Yamashita: Performed material characterization and contributed to data interpretation.
Fatimah Arofiaty Noor: Assisted in supervision and manuscript review.

Ferry Iskandar: Supervised the research, guided the methodology, and oversaw the overall project execution.

Conflicts of interest

The authors declare that they have no conflicts of interest.

Data and code availability

Research data are not shared.

Supplementary information

Supplementary information associated with this article is provided.

Ethical approval

Not applicable.

References

1. Simon P, Gogotsi Y (2020) Perspectives for electrochemical capacitors and related devices. Nat Mater 19:1151–1163. https://doi.org/10.1038/s41563-020-0747-z
2. Lim JM, Jang YS, Van T. Nguyen H, et al (2023) Advances in high-voltage supercapacitors for energy storage systems: materials and electrolyte tailoring to implementation. Nanoscale Adv 5:615–626. https://doi.org/10.1039/d2na00863g
3. Sadavar SV, Lee SY, Park SJ (2024) Advancements in Asymmetric Supercapacitors: From Historical Milestones to Challenges and Future Directions. Advanced Science 2403172:. https://doi.org/10.1002/advs.202403172
4. Chen Y, Yang H, Han Z, et al (2022) MXene-Based Electrodes for Supercapacitor Energy Storage. Energy and Fuels 36:2390–2406. https://doi.org/10.1021/acs.energyfuels.1c04104
5. Yusuf VF, Malek NI, Kailasa SK (2022) Review on Metal-Organic Framework Classification, Synthetic Approaches, and Influencing Factors: Applications in Energy, Drug Delivery, and Wastewater Treatment. ACS Omega 7:44507–44531. https://doi.org/10.1021/acsomega.2c05310
6. Abdillah OB, Jaoh FL, Fitriani P, et al (2024) A High-Performance, Low Defected, and Binder-Free Graphene-Based Supercapacitor Obtained via Synergistic Electrochemical Exfoliation and Electrophoretic Deposition Process. Chem Asian J 19:e202400548. https://doi.org/https://doi.org/10.1002/asia.202400548
7. Abdillah OB, Floweri O, Irham MA, et al (2022) Structural Modulation of Exfoliated Graphene via a Facile Postultrasonication Treatment toward Enhanced Electrochemical Properties of Supercapacitor Electrode. Energy & Fuels 36:14453–14463. https://doi.org/10.1021/acs.energyfuels.2c02809

8. Guo S, Guo B, Ma R, et al (2020) KOH activation of coal-derived microporous carbons for oxygen reduction and supercapacitors. RSC Adv 10:15707–15714. https://doi.org/10.1039/d0ra01705a

9. Song G, Romero C, Lowe T, et al (2023) Multistage Activation of Anthracite Coal-Based Activated Carbon for High-Performance Supercapacitor Applications. Energy and Fuels 37:1327–1343. https://doi.org/10.1021/acs.energyfuels.2c03487

10. Lu Q, Xu YY, Mu SJ, Li WC (2017) The effect of nitrogen and/or boron doping on the electrochemical performance of non-caking coal-derived activated carbons for use as supercapacitor electrodes. Xinxing Tan Cailiao/New Carbon Materials 32:442–450. https://doi.org/10.1016/S1872-5805(17)60133-1

11. Ngidi NPD, Koekemoer AF, Ndlela SS (2024) Recent advancement in the electrochemical performance of electrochemical capacitors based on biomass-derived porous carbon: A review. J Energy Storage 89:111638. https://doi.org/10.1016/j.est.2024.111638

12. Bora M, Bhattacharjya D, Saikia BK (2021) Coal-Derived Activated Carbon for Electrochemical Energy Storage: Status on Supercapacitor, Li-Ion Battery, and Li-S Battery Applications. Energy and Fuels 35:18285–18307. https://doi.org/10.1021/acs.energyfuels.1c02518

13. Li L, Sun F, Gao J, et al (2018) Broadening the pore size of coal-based activated carbon: Via a washing-free chem-physical activation method for high-capacity dye adsorption. RSC Adv 8:14488–14499. https://doi.org/10.1039/c8ra02127a

14. Elmouwahidi A, Bailón-García E, Romero-Cano LA, et al (2019) Influence of surface chemistry on the electrochemical performance of biomass-derived carbon electrodes for its use as supercapacitors. Materials 12:. https://doi.org/10.3390/ma12152458

15. Thakur AK, Kurtyka K, Majumder M, et al (2022) Recent Advances in Boron- and Nitrogen-Doped Carbon-Based Materials and Their Various Applications. Adv Mater Interfaces 9:. https://doi.org/10.1002/admi.202101964

16. Paraknowitsch JP, Thomas A (2013) Doping carbons beyond nitrogen: An overview of advanced heteroatom doped carbons with boron, sulphur and phosphorus for energy applications. Energy Environ Sci 6:2839–2855. https://doi.org/10.1039/c3ee41444b

17. Mehare RS, Chaturvedi V, Shelke M V. (2021) Synthesis and structural/electrochemical evaluation of N, S co-doped activated porous carbon spheres as efficient electrode material for supercapacitors. Electrochemical Science Advances 1:1–10. https://doi.org/10.1002/elsa.202000021

18. Jiang Q, Cai Y, Sang X, et al (2024) Nitrogen-Doped Carbon Materials As Supercapacitor Electrodes : A Mini Review. https://doi.org/10.1021/acs.energyfuels.4c00918

19. Ismagilov ZR, Shalagina AE, Podyacheva OY, et al (2009) Structure and electrical conductivity of nitrogen-doped carbon nanofibers. Carbon N Y 47:1922–1929. https://doi.org/10.1016/j.carbon.2009.02.034

20. Das TK, Banerjee S, Kumar A, et al (2022) Nitrogen-doped hierarchically porous carbon obtained via single step method for high performance supercapacitors. Int J Hydrogen Energy 47:12829–12840. https://doi.org/10.1016/j.ijhydene.2022.02.036

21. Yang M, Zhou Z (2017) Recent Breakthroughs in Supercapacitors Boosted by Nitrogen-Rich Porous Carbon Materials. Advanced Science 4:1–10. https://doi.org/10.1002/advs.201600408

22. Inagaki M, Toyoda M, Soneda Y, Morishita T (2018) Nitrogen-doped carbon materials. Carbon N Y 132:104–140. https://doi.org/10.1016/j.carbon.2018.02.024

23. Cao YJ, Lu CY, Zhang ZW, et al (2022) N/O Co-doped Porous Carbons Derived from Coal Tar Pitch for Ultra-high Specific Capacitance Supercapacitors. ACS Omega 7:23342–23352. https://doi.org/10.1021/acsomega.2c01534

24. Liu A, Yan L, Zhang Y, et al (2024) Nitrogen-doped coal-based microporous carbon material co-activated by HCOOK and urea for high performance supercapacitors. Surfaces and Interfaces 44:103754. https://doi.org/10.1016/j.surfin.2023.103754

25. Li KK, Liu GY, Zheng LS, et al (2021) Coal-derived carbon nanomaterials for sustainable energy storage applications. Xinxing Tan Cailiao/New Carbon Materials 36:133–154. https://doi.org/10.1016/S1872-5805(21)60010-0

26. Ye C ping, Huang H jun, Li X hong, et al (2017) The oxygen evolution during pyrolysis of HunlunBuir lignite under different heating modes. Fuel 207:85–92. https://doi.org/10.1016/j.fuel.2017.06.062

27. Wang C, Zeng F, Li C, et al (2024) Insight into the molecular structural evolution of a series of medium-rank coals from China by XRD, Raman and FTIR. J Mol Struct 1303:137616. https://doi.org/10.1016/j.molstruc.2024.137616

28. Fang X, Wu C, Song Y, et al (2024) The impact of pyrolysis temperature on the evolution of the maceral and mineral geochemistry in a subbituminous coal. Energy 290:130092. https://doi.org/10.1016/j.energy.2023.130092

29. Li M, Zeng F, Chang H, et al (2013) Aggregate structure evolution of low-rank coals during pyrolysis by in-situ X-ray diffraction. Int J Coal Geol 116–117:262–269. https://doi.org/10.1016/j.coal.2013.07.008

30. Xu J, Xiang X, Xu K, et al (2021) Developing micro-Raman spectroscopy for char structure characterization in the scale of micro- and bulk: A case study of Zhundong coal pyrolysis. Fuel 291:120168. https://doi.org/10.1016/j.fuel.2021.120168

31. Meng D, Yue C, Wang T, Chen X (2021) Evolution of carbon structure and functional group during Shenmu lump coal pyrolysis. Fuel 287:119538. https://doi.org/10.1016/j.fuel.2020.119538

32. Tian QQ, Li XM, Xie LJ, et al (2023) Insights into the carbonization mechanism of bituminous coal-derived carbon materials for lithium-ion and sodium-ion batteries. Xinxing Tan Cailiao/New Carbon Materials 38:939–953. https://doi.org/10.1016/S1872-5805(23)60759-0

33. Anrokhi MS, Abdillah OB, Fitriani P, et al (2024) Preliminary Study of Carbonized Bituminous Raw Coal for Supercapacitor Electrode. J Phys Conf Ser 2734:. https://doi.org/10.1088/1742-6596/2734/1/012022

34. Xiong G, He P, Lyu Z, et al (2018) Bioinspired leaves-on-branchlet hybrid carbon nanostructure for supercapacitors. Nat Commun 9:. https://doi.org/10.1038/s41467-018-03112-3

35. Dun W, Guijian L, Ruoyu S, Xiang F (2013) Investigation of structural characteristics of thermally metamorphosed coal by FTIR spectroscopy and X-ray diffraction. Energy and Fuels 27:5823–5830. https://doi.org/10.1021/ef401276h

36. Insiripong S, Kedkaew C, Thamaphat K, Chantima N (2012) Irradiation effect on natural quartz from Zambia. Procedia Eng 32:83–89. https://doi.org/10.1016/j.proeng.2012.01.1240

37. Liu M, Bai J, Kong L, et al (2020) The correlation between coal char structure and reactivity at rapid heating condition in TGA and heating stage microscope. Fuel 260:116318. https://doi.org/10.1016/j.fuel.2019.116318

38. Yin Y, Wu Z, Tao J, et al (2022) Investigation of the Evolution of the Chemical Structure of Bituminous Coals and Lignite during Pyrolysis. Crystals (Basel) 12:. https://doi.org/10.3390/cryst12040444

39. Sonibare OO, Haeger T, Foley SF (2010) Structural characterization of Nigerian coals by X-ray diffraction, Raman and FTIR spectroscopy. Energy 35:5347–5353. https://doi.org/10.1016/j.energy.2010.07.025

40. Ren L, Zhang K, Wang F, et al (2024) Carbon structure evolution of coal slime under different pyrolysis methods: Quantitative analysis of carbon structure and finite-element simulation calculations. Fuel 357:130048. https://doi.org/10.1016/j.fuel.2023.130048

41. Liu S, Zhang Y, Tuo K, et al (2018) Structure, electrical conductivity, and dielectric properties of semi-coke derived from microwave-pyrolyzed low-rank coal. Fuel Processing Technology 178:139–147. https://doi.org/10.1016/j.fuproc.2018.05.028

42. Hu J, Chen Y, Qian K, et al (2017) Evolution of char structure during mengdong coal pyrolysis: Influence of temperature and K2CO3. Fuel Processing Technology 159:178–186. https://doi.org/10.1016/j.fuproc.2017.01.042

43. Iskandar F, Abdillah OB, Mayangsari TR, Aimon AH (2018) Preliminary Study of Graphite Rod Pre-treatment in H2O2/H2SO4 Mixture Solution on the Synthesized Graphene by Electrochemical Exfoliation Method. In: 2018 5th International Conference on Electric Vehicular Technology (ICEVT). pp 46–48

44. Björkman Å (1969) Thermische Klärschlammbehandlung. Schweizerische Zeitschrift für Hydrologie 31:632–645. https://doi.org/10.1007/BF02543692

45. He X, Liu X, Nie B, Song D (2017) FTIR and Raman spectroscopy characterization of functional groups in various rank coals. Fuel 206:555–563. https://doi.org/10.1016/j.fuel.2017.05.101

46. Sadezky A, Muckenhuber H, Grothe H, et al (2005) Raman microspectroscopy of soot and related carbonaceous materials: Spectral analysis and structural information. Carbon N Y 43:1731–1742. https://doi.org/10.1016/j.carbon.2005.02.018

47. Sood AK, Gupta R, Asher SA (2001) Origin of the unusual dependence of Raman D band on excitation wavelength in graphite-like materials. J Appl Phys 90:4494–4497. https://doi.org/10.1063/1.1408590

48. Wang Y, Alsmeyer DC, McCreery RL (1990) Raman Spectroscopy of Carbon Materials: Structural Basis of Observed Spectra. Chemistry of Materials 2:557–563. https://doi.org/10.1021/cm00011a018

49. Al-Jishi R, Dresselhaus G (1982) Lattice-dynamical model for graphite. Phys Rev B 26:4514–4522. https://doi.org/10.1103/PhysRevB.26.4514

50. Li K, Cao H, Rimmer SM, et al (2023) Petrographic features and carbon structural evolution of a series of high-temperature treated anthracites. Int J Coal Geol 277:104356. https://doi.org/10.1016/j.coal.2023.104356

51. TUINSTRA F, KOENIG JL (1970) Raman Spectrum of Graphite. Journal of Chemical Physics 53:1126–1130. https://doi.org/10.1063/1.1674108

52. Yu J, Guo Q, Ding L, et al (2020) Studying effects of solid structure evolution on gasification reactivity of coal chars by in-situ Raman spectroscopy. Fuel 270:117603. https://doi.org/10.1016/j.fuel.2020.117603

53. Liu H, Chen T, Fang L (2020) Evolution of char structure during non-isothermal low temperature pyrolysis of ZhunDong coal by microwave heating: A comparative study with conventional heating. Journal of the Energy Institute 93:1195–1206. https://doi.org/10.1016/j.joei.2019.11.003

54. Seo DK, Park SS, Kim YT, et al (2011) Study of coal pyrolysis by thermo-gravimetric analysis (TGA) and concentration measurements of the evolved species. J Anal Appl Pyrolysis 92:209–216. https://doi.org/10.1016/j.jaap.2011.05.012

55. Liu H, Jin Z, An L, et al (2025) A Reproducible and Self-Repairable Ionic Skin with Robust Performance Retention Enabled by Modulating the Noncovalent Interactions. ACS Appl Polym Mater 7:1459–1470. https://doi.org/10.1021/acsapm.4c03195

56. Pels JR, Kapteijn F, Moulijn JA, et al (1995) Evolution of nitrogen functionalities in carbonaceous materials during pyrolysis. Carbon N Y 33:1641–1653. https://doi.org/10.1016/0008-6223(95)00154-6

57. Kelemen SR, Gorbaty ML, Kwiatek PJ, et al (1998) Nitrogen transformations in coal during pyrolysis. Energy and Fuels 12:159–173. https://doi.org/10.1021/ef9701246

58. Tian Q, Li X, Xie L, et al (2023) Insights into the carbonization mechanism of bituminous coal-derived carbon materials for lithium-ion and sodium- ion batteries. New Carbon Materials 38:939–953. https://doi.org/10.1016/S1872-5805(23)60759-0

59. Hulicova D, Kodama M, Hatori H (2006) Electrochemical performance of nitrogen-enriched carbons in aqueous and non-aqueous supercapacitors. Chemistry of Materials 18:2318–2326. https://doi.org/10.1021/cm060146i

60. Ornelas O, Sieben JM, Ruiz-Rosas R, et al (2014) On the origin of the high capacitance of nitrogen-containing carbon nanotubes in acidic and alkaline electrolytes. Chemical Communications 50:11343–11346. https://doi.org/10.1039/c4cc04876h

61. Castro-Muñiz A, Hoshikawa Y, Kasukabe T, et al (2016) Real Understanding of the Nitrogen-Doping Effect on the Electrochemical Performance of Carbon Materials by Using Carbon-Coated Mesoporous Silica as a Model Material. Langmuir 32:2127–2135. https://doi.org/10.1021/acs.langmuir.5b03667

62. Treeweranuwat P, Boonyoung P, Chareonpanich M, Nueangnoraj K (2020) Role of Nitrogen on the Porosity, Surface, and Electrochemical Characteristics of Activated Carbon. ACS Omega 5:1911–1918. https://doi.org/10.1021/acsomega.9b03586

63. Zhao P, Shen B, Yang M, et al (2023) Effect of nitrogen species on electrochemical properties of N-doped carbon nanotubes derived from co-pyrolysis of low-density polyethylene and melamine. J Energy Storage 67:107569. https://doi.org/10.1016/j.est.2023.107569

64. Li YT, Pi YT, Lu LM, et al (2015) Hierarchical porous active carbon from fallen leaves by synergy of K2CO3 and their supercapacitor performance. J Power Sources 299:519–528. https://doi.org/10.1016/j.jpowsour.2015.09.039

65. Lin JH (2018) The influence of the interlayer distance on the performance of thermally reduced graphene oxide supercapacitors. Materials 11:. https://doi.org/10.3390/ma11020263